Title

Functional interferometric diffusing wave spectroscopy of the human brain

Journal

Science Advances, 7(20)

ISSN

2375-2548

Authors

Zhou, Wenjun
Kholiqov, Oybek
Zhu, Jun
et al.

Publication Date

2021-05-14

DOI

10.1126/sciadv.abe0150

Peer reviewed

OPTICS

Functional interferometric diffusing wave spectroscopy of the human brain

Wenjun Zhou[1], Oybek Kholiqov[1], Jun Zhu[1], Mingjun Zhao[1], Lara L. Zimmermann[2], Ryan M. Martin[2], Bruce G. Lyeth[2], Vivek J. Srinivasan[1,3,4,5,6]*

Cerebral blood flow (CBF) is essential for brain function, and CBF-related signals can inform us about brain activity. Yet currently, high-end medical instrumentation is needed to perform a CBF measurement in adult humans. Here, we describe functional interferometric diffusing wave spectroscopy (fiDWS), which introduces and collects near-infrared light via the scalp, using inexpensive detector arrays to rapidly monitor coherent light fluctuations that encode brain blood flow index (BFI), a surrogate for CBF. Compared to other functional optical approaches, fiDWS measures BFI faster and deeper while also providing continuous wave absorption signals. Achieving clear pulsatile BFI waveforms at source-collector separations of 3.5 cm, we confirm that optical BFI, not absorption, shows a graded hypercapnic response consistent with human cerebrovascular physiology, and that BFI has a better contrast-to-noise ratio than absorption during brain activation. By providing high-throughput measurements of optical BFI at low cost, fiDWS will expand access to CBF.

INTRODUCTION

Comprising 2% of the body weight in adults, the human brain commands around 15 to 20% of the basal cardiac output as cerebral blood flow (CBF) (*1*). Deficiencies of CBF and resulting ischemia are causes of primary or secondary injury in numerous neurological disorders, including acute stroke (*2*), intraparenchymal hemorrhage (*3*), traumatic brain injury (*4*), and subarachnoid hemorrhage (*5*). In addition, because CBF is routed to active brain regions through neurovascular coupling (*6*), signals related to CBF increments can also indirectly monitor brain activity (*7*). The most well-known such signal is blood oxygenation level-dependent (BOLD) functional magnetic resonance imaging (fMRI) (*8*, *9*), a cornerstone of functional neuroimaging, and the basis for high-performance, noninvasive, brain computer interfaces (*10*).

Although neuroimaging of CBF (*11*, *12*) is used to assess brain injury and recovery in neurointensive care, the role of CBF monitoring is limited as it is usually not continuous and acquired by expensive MRI (*13*) and computed tomography scanners (*14*). Transcranial Doppler ultrasound (*15*) is quasi-continuous but measures macrovessel velocity, not microvascular flow, and can be position-dependent and challenging in many subjects, even with a skilled operator. Fortunately, near-infrared (NIR) light, when introduced via the scalp, propagates diffusively into the adult human brain (*16*, *17*) before reemerging from the scalp, where it can be collected and measured. Conventional NIR spectroscopy (NIRS) assesses absorption of this light to determine hemoglobin concentrations or their changes (*18*). In a related physical process, temporal fluctuations of scattered coherent light encode red blood cell dynamics in the tissue traversed by the NIR light (*19*). Diffusing wave spectroscopy (DWS) and diffuse correlation spectroscopy (DCS) quantify intensity fluctuations (*20*, *21*), deriving a blood flow index (BFI) that serves as a surrogate for conventional blood flow (*22*–*27*).

The ability to introduce and collect light noninvasively via the scalp is a strength of optical techniques. However, it is also the source of an important limitation, namely, that extracerebral "clutter" from tissue traversed by NIR light can contaminate the desired brain signals (*28*). Extracerebral contamination can confound results in neurosurgery, if weakly regulated scalp blood flow is mistaken for dysregulated CBF (*29*), or in a brain-computer interface, where an incorrect decision is made in response to a systemic, corrupting physiological change. Thus, approaches to mitigate this contamination have been proposed, including probe pressure (*30*, *31*), superficial regression (*32*), time-of-flight discrimination (*33*, *34*), depth discrimination (*35*–*37*), and increased source-collector (S-C) separation (*38*), each with limitations.

Studies have concluded that if extracerebral contamination is the main concern, then BFI, not hemoglobin, is, at least theoretically, a better signal. Specifically, optical fluctuations (i.e., DWS/DCS) achieve 3 to 5× better brain sensitivity than optical absorption (i.e., NIRS) (*38*, *39*), primarily because brain BFI exceeds extracerebral BFI by 6 to 10×, while the corresponding ratio for hemoglobin is only about 2.5× (*38*). Thus, another approach to mitigate extracerebral contamination is to measure BFI rather than hemoglobin (Fig. 1).

However, despite the theoretical intrinsic advantages of BFI, hemoglobin absorption signals are far more widely used in practice (*40*). This is because DWS/DCS can only effectively measure a small number of spatial modes, or speckle grains, per detector (*41*), while NIRS can effectively measure many spatial modes. Since the surface flux of returning light that penetrates to the brain through the skull and scalp is weak, DWS/DCS needs either long integration times or many expensive, single photon counting channels with single mode collectors. As shown in Fig. 1, increasing S-C separation by 1 cm asymptotically reduces collected light by roughly an order of magnitude. Thus, compared to conventional NIRS (*40*), which can use large light collectors, in DWS/DCS, S-C separations are restricted (*42*), in turn, reducing brain specificity. Parallelization is possible but prohibitively expensive (*43*). Thus, the theoretical advantages of BFI (*38*, *39*) as a brain signal have not been fully realized. By

[1]Department of Biomedical Engineering, University of California, Davis, Davis, CA, USA. [2]Department of Neurological Surgery, University of California, Davis, Sacramento, CA, USA. [3]Department of Ophthalmology and Vision Science, University of California, Davis, Sacramento, CA, USA. [4]Department of Ophthalmology, NYU Langone Health, New York, NY, USA. [5]Department of Radiology, NYU Langone Health, New York, NY, USA. [6]Tech4Health Institute, NYU Langone Health, New York, NY, USA.
*Corresponding author. Email: vjsriniv@ucdavis.edu

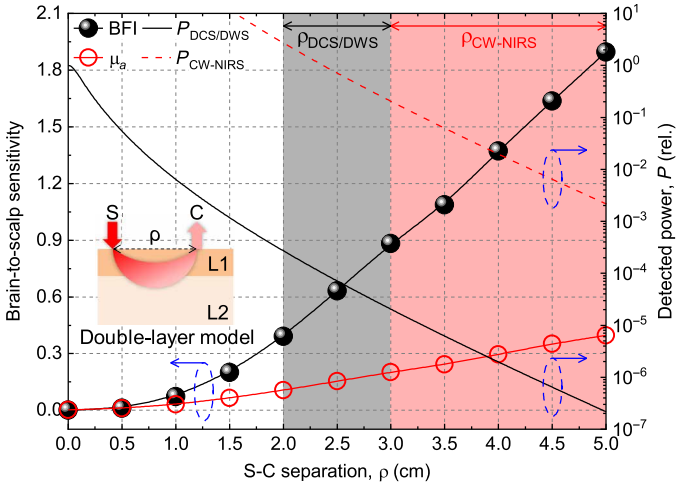

Fig. 1. Brain-to-scalp sensitivity of optical BFI (DCS/DWS) exceeds that of absorption (CW-NIRS). The brain-to-scalp sensitivities of optical BFI and optical absorption (μ_a) measurements were simulated (section S5) with a double-layer model (inset), with extracerebral and cerebral layers designated as "scalp" and "brain" for short. Optical BFI is intrinsically more brain specific than absorption, achieving a higher brain-to-scalp sensitivity at a given S-C separation. However, the remitted light flux and detected power (right *y* axis) decrease approximately exponentially with increasing S-C separation, which is needed for high brain-to-scalp sensitivity. Because of the expense of single or few mode photon-counting channels, required for coherence, DCS/DWS uses relatively short S-C separations (black shading). On the other hand, CW-NIRS can collect many modes that sum incoherently and therefore can use larger S-C separations (red shading). We assume that $P_{CW-NIRS}$ is $10^4 \times P_{DCS/DWS}$, based on a hypothetical CW-NIRS system that collects 10^4 modes for every single DCS/DWS mode. Blue dashed ovals with arrows point to corresponding *y* axes. Inset: ρ (S-C separation), L1 (extracerebral layer), and L2 (cerebral layer). Note that in practice, effective brain-to-scalp sensitivity can be further improved by considering additional superficial short S-C channels in signal analysis.

comparison, NIRS can compare short and long S-C channels to mitigate the problem of superficial contamination through signal processing (*44*) and remains the optical method of choice for functional brain measurements.

Here, we present functional interferometric DWS (fiDWS), which assesses BFI changes specific to brain physiology via the in-phase field fluctuations of NIR light. Leveraging multimode fiber collection and interferometry with single-mode reference light shaping while optimizing the inherently parallel detection of a complementary metal-oxide semiconductor (CMOS) sensor (*45*) through design and postprocessing, our method eliminates photon counting, which is associated with high cost (*46*), while also boosting performance. We engineer and optimize an fiDWS system (comprising a source, interferometer, optodes, data streaming, and software for real-time display and postprocessing) with >50× higher light throughput-to-cost ratio than DWS/DCS, enabling measurement of autocorrelations at S-C separations of up to 5.0 cm in the adult human head with a 10-s integration time. We proceed to investigate BFI pulsatility, changes during brain activation, and carbon dioxide (CO_2) reactivity at S-C separations of 3.5 cm, with a 0.1-s integration time, in multiple subjects. We demonstrate that with advances in throughput, fiDWS can perform continuous-wave (CW) intensity measurements, which serve as both a gold standard for comparison and a tool to improve accuracy of estimated BFI changes. The results support that fiDWS achieves record brain specificity, providing an approach that experimentally realizes the advantages, heretofore theoretical, of the functional BFI signal.

RESULTS

Characterization of fiDWS system performance

Noninvasive optical technologies to measure fluctuation signals in adult humans must sense coherent, very weak light fluxes that return from the cerebral cortex or subcortical white matter, approximately 1.5 to 2 cm below the scalp. Because of the limited light budget, S-C separations of conventional optical flowmetry are restricted to the regime where brain-to-scalp sensitivity is less than unity (Fig. 1).

In fiDWS (Fig. 2A), we use interferometry, which boosts the weak optical field returning from the brain by a strong reference field (see Materials and Methods). Therefore, a CMOS sensor can replace photon counting and parallelize measurements of weak diffuse light fluctuations that reveal CBF while still achieving the shot noise limit (section S1). Previous optical BFI systems, including DCS/DWS (*42*, *43*) and a preliminary iDWS proof of concept (*45*), performed high-speed (pulsatile) monitoring at S-C separations of 2.5 to 2.9 cm. For this study, we designed and built a multimode fiDWS system to measure pulsatile BFI at S-C separations up to 3.5 to 4.0 cm (depending on the subject), where the remitted light is an order of magnitude smaller. Innovations needed to achieve these results included a bulk interferometer (Fig. 2A) that enabled a single-mode reference arm with a Powell lens for nearly uniform heterodyne gain (Fig. 2B), a sample collection fiber with a larger core and higher numerical aperture (NA) for more sample modes, optimized processing (including binning and rolling reference subtraction) (see Materials and Methods and fig. S2), and software for real-time processing, display, and streaming (section S3). Theoretical considerations needed for these experiments, including a simple expression for brain-to-scalp sensitivity (section S4), a method to estimate the zero lag autocorrelation derivative that is specific for brain BFI (see Materials and Methods and section S4) and the effect of the finite camera exposure time on the autocorrelation function (section S5), are also described here.

Coherent detection systems are affected by both speckle noise and additive noise. Thus, two important metrics determine iDWS performance: speckle number ($N_{Speckle}$) and signal–to–additive noise ratio (SANR) (*45*), where additive noise is ideally dominated by shot noise from the reference arm (section S1). In the limit of short S-C separation, signal levels are high, and it is beneficial to minimize speckle noise; hence, a large $N_{Speckle}$ is required. However, for fiDWS of the human brain, large S-C separations are required, where shot noise from the reference arm, not speckle noise, is the dominant noise source. In addition, since adjacent pixels measure partially correlated signals, binning can reduce noise in autocorrelation estimates by coherently adding correlated signals, while uncorrelated noise adds incoherently. Here, we target maximization of signal-to-noise ratio (SNR) of the autocorrelation estimate as the ultimate goal. In contrast to our prior work that used ad hoc rectangular window pixel binning (*45*), here, we derived both the optimal binning function and the optimal autocorrelation SNR (sections S6 and S7).

Using a prior, suboptimal, nonoverlapping, rectangular window pixel binning method (*45*), our new system markedly outperforms

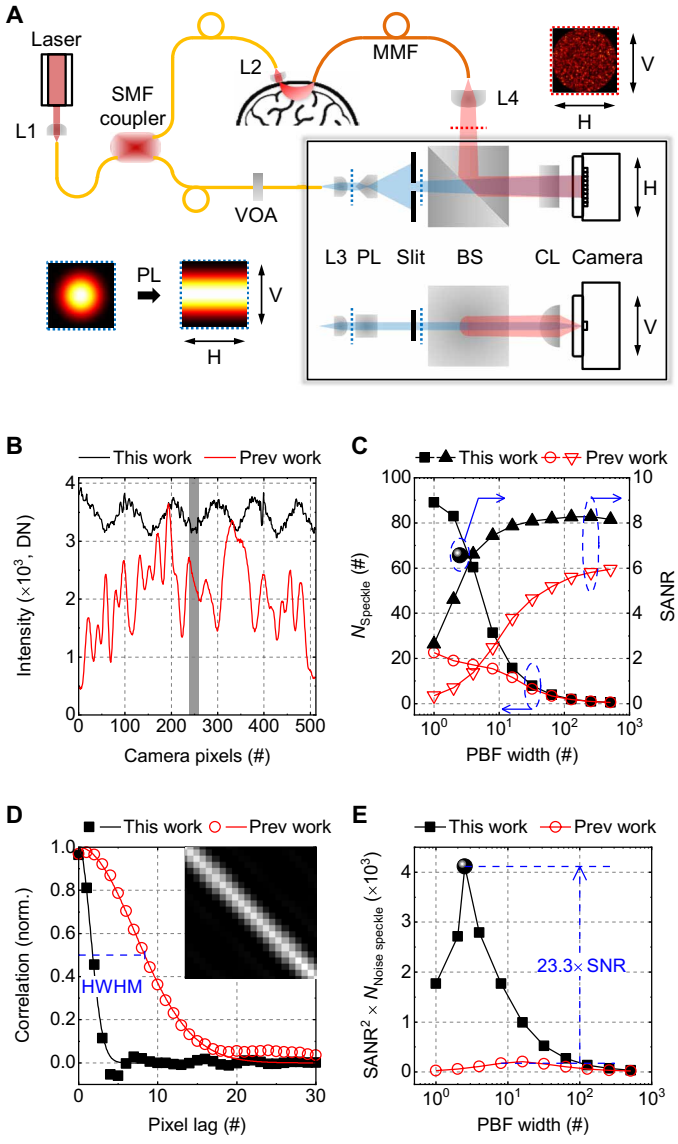

Fig. 2. fiDWS for optical BFI in the human brain. (**A**) Schematic of fiDWS. The interferometer detection path is shown in both horizontal (H) and vertical (V) views. Transverse intensity distributions of sample and reference light, at positions indicated by red and blue dotted lines, are shown (insets) with correspondingly colored dotted frames. SMF, single-mode fiber; MMF, multimode fiber; L1 to L4, lenses; VOA, variable fiber-optic attenuator; PL, Powell lens; BS, beamsplitter; CL, cylindrical lens. (**B**) Intensity patterns of reference light used in this work (black) and previous work (*45*) (red). DN, digital number. (**C**) Comparisons of estimated $N_{Speckle}$ (squares and circles) and SANR (triangles) versus width of rectangular window used for pixel binning. Corresponding SANR (for this work), based on optimized pixel binning (fig. S5), is indicated by the spherical symbol. Blue dashed ovals with arrows point to corresponding *y* axes. (**D**) Spatial correlation of heterodyne signals across pixels (scatters) and corresponding Gaussian fits (solid curves). Inset shows the correlation matrix of the current system within the gray shaded region in (B). HWHM, half width at half maximum. (**E**) Comparison of $SANR^2 \times N_{Noise\ speckle}$, a metric for fiDWS system performance that is proportional to the autocorrelation SNR. The spherical symbol shows the fiDWS results with optimized data processing (see also section S6 and fig. S5), achieving a ~23.3 times improvement compared to (*45*). Note that comparisons in (C) to (E) are based on phantom measurements with the same S-C separation.

the previous system (*45*) both in terms of speckle number (corrected for additive noise as described in Materials and Methods and section S8) and SANR (Fig. 2C). As expected, with varying degrees of binning, a strong trade-off between $N_{Speckle}$ and SANR is evident. Here, we draw a distinction between the raw measurement SANR of the heterodyne signals and the SNR of the autocorrelation from which blood flow dynamics are derived. As might be expected, the autocorrelation SNR depends on the raw measurement SANR; precisely, the autocorrelation SNR is proportional to the product of $SANR^2$ and the number of noise speckles ($N_{Noise\ speckle}$; section S6). We take this quantity as a metric of fiDWS performance. Pixel binning increases the SANR while reducing $N_{Noise\ speckle}$ relative to its maximal value (fig. S5). Here, we show that the optimal sliding pixel binning function, which maximizes the $SANR^2 \times N_{Noise\ speckle}$ metric and hence the autocorrelation SNR, has a spatial correlation equal to the raw spatial correlation of heterodyne signals across camera pixels (Fig. 2D and fig. S5). This optimal binning function, which is approximately Gaussian with a 2.5-pixel width (Δp_{PBF}; eq. S32), enables a further autocorrelation SNR improvement of ~1.5 relative to the prior nonoverlapping rectangular binning approach. With this multitude of experimental and theoretical advances, the autocorrelation SNR is enhanced by ~23.3 times (Fig. 2E), relative to the best prior results (*45*). This results from improvements in both $N_{Noise\ speckle}$ (from ~29 to ~96) and SANR (~2.65×), propelling fiDWS performance beyond that of existing optical BFI methodologies.

We next proceeded to investigate how BFI, from a semi-infinite homogenous model, and SANR (proportional to collected sample power in the shot noise limit) change with S-C separation (Fig. 3A). Clear pulsatile BFI traces are obtained up to 3.5-cm S-C separations (Fig. 3B). The quality of the pulsatile waveform appears comparable to state-of-the-art DCS/DWS at 2.9-cm S-C separation, which used many (14) expensive photon-counting channels (*43*). Even at 3.5-cm S-C separation, the quality of the pulsatile waveform is sufficient to enable self-alignment of BFI traces with respect to the cardiac cycle. At 4.0-cm S-C separation, heart rate (HR) is resolvable in the fast Fourier transform (Fig. 3F). For one subject, an S-C separation of 5.0 cm was tested, where field autocorrelations were measurable with a 10-s integration time (Fig. 3C). At such large S-C separations, decorrelation during the exposure time must be accounted for in quantitative analysis (section S5), and the early portion of the autocorrelation decay was undersampled (although this issue could be solved with megahertz cameras). Given these issues, extreme S-C separations beyond 4.0 cm were not pursued further. BFIs, from fitting $G_1(\tau_d)$ with a semi-infinite DCS model (see Materials and Methods), and SANRs, from noise-corrected $G_1(0)$, were averaged across forehead locations in four subjects at S-C separations from 1.0 to 4.0 cm (Fig. 3, D and E). Overall, BFI increased and SANR decreased with increasing S-C separation. Moreover, the coefficient of variation of BFI, across subjects and locations, decreased with increasing S-C separation, while the coefficient of variation of SANR (collected sample power), similarly defined, increased with increasing S-C separation. More consistent BFI values at large S-C separations may be due to the larger volume probed and lower susceptibility to heterogeneous scalp flow and differences in applied pressure. Last, larger variability in collected sample power at larger S-C separations may relate to differences in optical properties across measured subjects and locations, which affect the collected light levels more at larger path lengths.

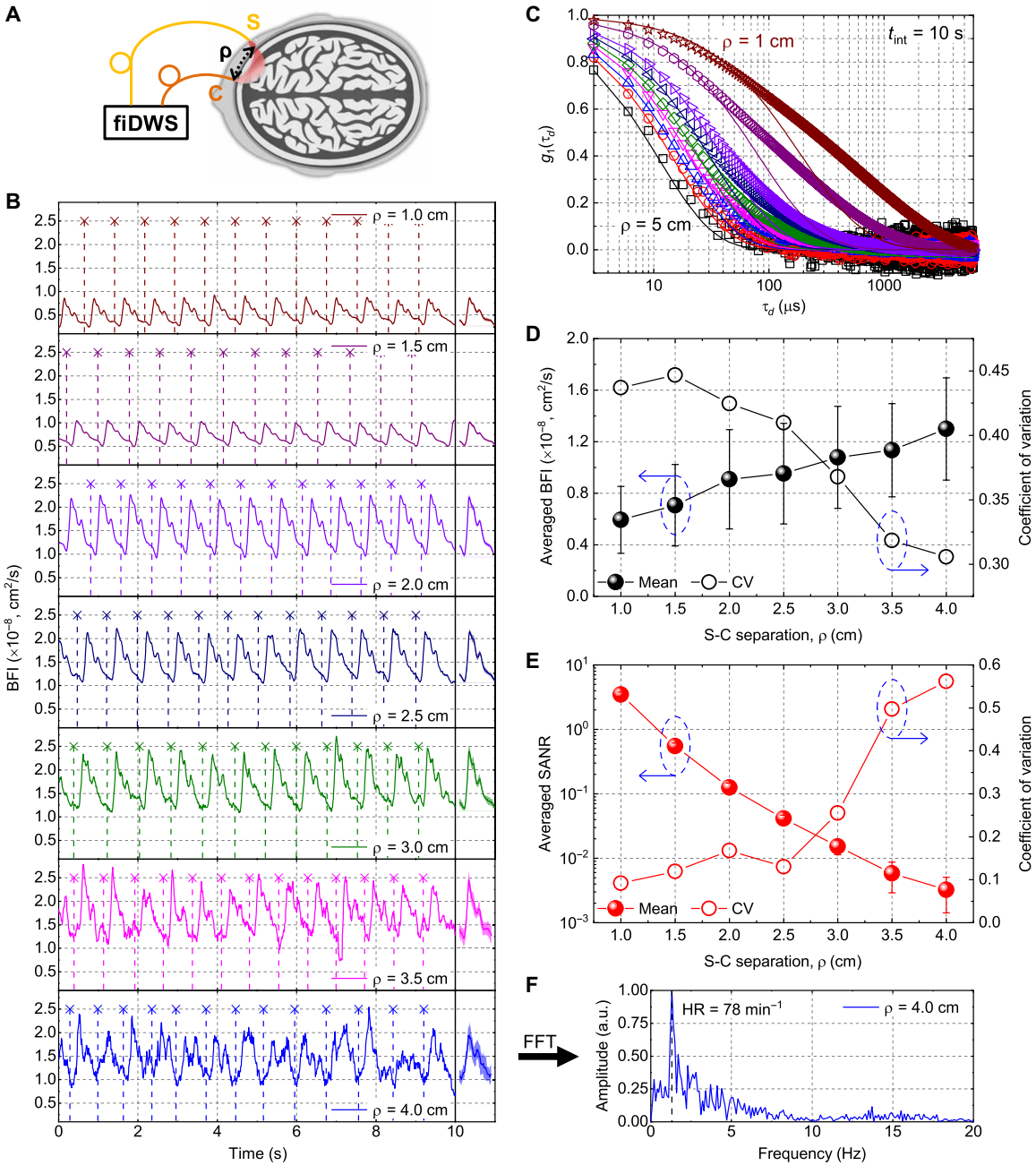

Fig. 3. fiDWS monitors pulsatile BFI at 3.5-cm S-C separation and autocorrelations at up to 5-cm S-C separation from the adult human forehead. (**A**) Schematic of human brain measurements. (**B**) Pulsatile BFI traces from a single subject with S-C separations from 1 to 4 cm. Temporal sampling and integration time are 0.01 and 0.1 s, respectively. Vertical dashes show estimated boundaries of BFI pulses corresponding to heartbeats. The heartbeat-averaged BFI waveforms [standard deviations (SDs) shaded] follow the BFI traces. (**C**) Normalized field autocorrelations [$g_1(\tau_d)$] at multiple S-C separations from 1 to 5 cm for the same subject in (B) (open symbols), with an integration time of 10 s. Solid curves show semi-infinite DCS model fits. (**D** and **E**) Averaged BFI (D) and SANR (E) versus S-C separation from multiple forehead locations across multiple subjects. Error bars indicate SDs. Corresponding coefficients of variation (CV; right *y* axes) are shown for averaged BFI (D) and SANR (E). Blue dashed ovals around symbols with arrows point to corresponding *y* axes. (**F**) Fast Fourier transform (FFT) spectrum of pulsatile BFI trace at 4-cm S-C separation (B) shows a peak (dashed line) at the HR of 78 min^{-1}. a.u., arbitrary units.

Validation of fiDWS for CW intensity measurements

DCS/DWS and NIRS provide complementary and synergistic information on optical blood flow and absorption. Although DCS/DWS can measure intensity (*47*, *48*), the brain specificity of optical absorption is limited at the typical DCS S-C separations of 2.5 cm used for the human head (*49*, *50*) (Fig. 1), and this signal is typically discarded, although it is sometimes useful in phantoms (*51*). Instead, for the human brain, researchers have investigated multimodal devices with separate NIRS and DCS systems (*38*). While such an approach affords larger S-C separations to enable more brain-specific

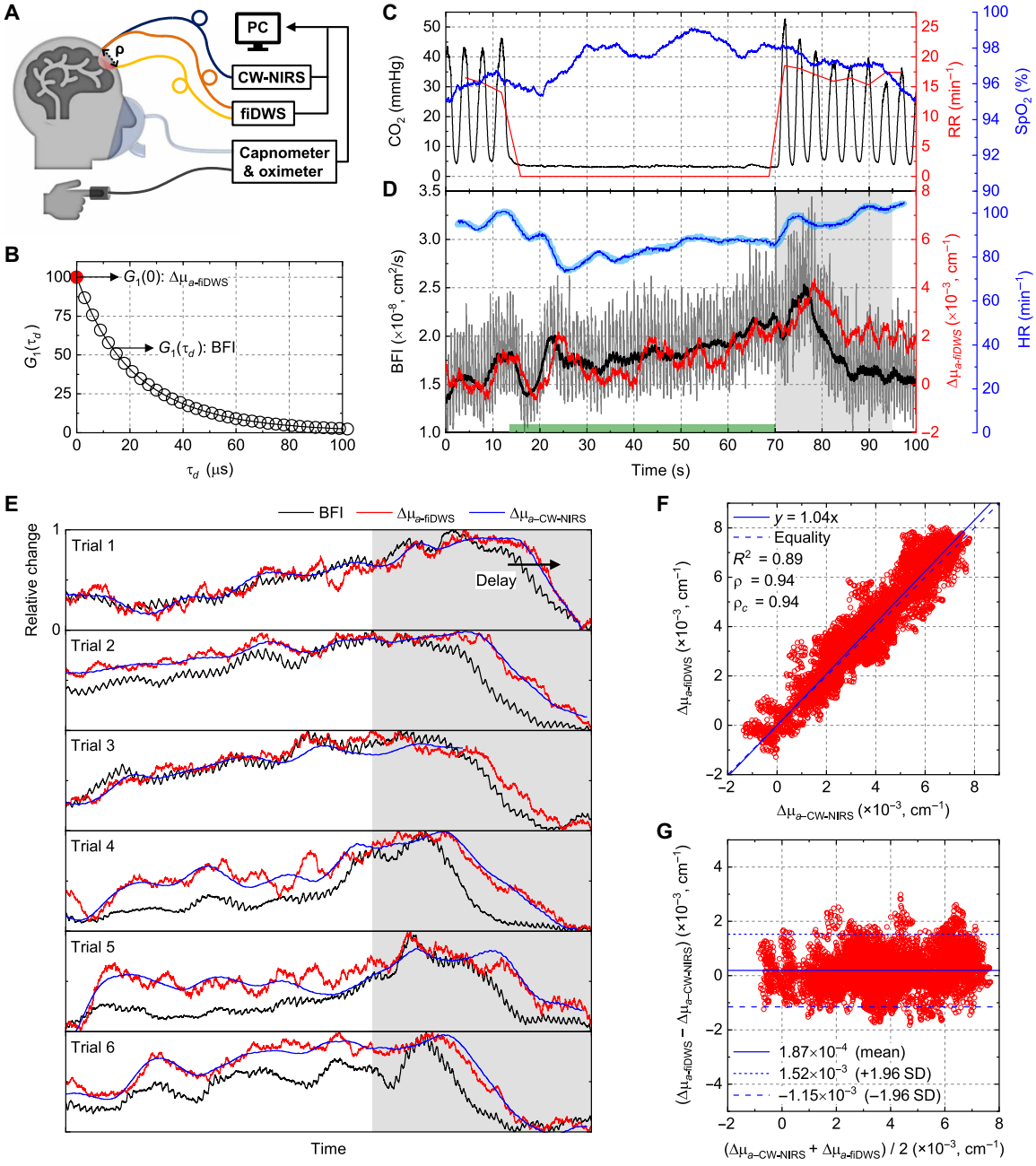

Fig. 4. fiDWS monitors CW light intensity. (**A**) Schematic of simultaneous fiDWS and CW-NIRS measurements during voluntary apnea (VA). (**B**) BFI and absorption can be determined from the noise-corrected field autocorrelation function, $G_1(\tau_d)$. (**C**) CO_2 waveform measured by capnometer and estimated respiration rate (RR) during a single VA trial. Oxygen saturation (SpO_2) was measured by a fingertip pulse oximeter. (**D**) BFI traces with (gray) and without (black) pulsatility, fitted from $G_1(\tau_d)$ with integration times of 0.1 and 2 s, respectively, were derived from a semi-infinite DCS model. Corresponding absorption changes ($\Delta\mu_{a-\text{fiDWS}}$) were estimated from changes in noise-corrected $G_1(0)$ with a 2-s integration time. HR, estimated from pulsatile BFI (blue), agrees with HR measured by the oximeter (light blue). Green bar on *x* axis indicates the VA period. (**E**) Rescaled BFI and $\Delta\mu_{a-\text{fiDWS}}$ (each normalized to [0, 1]), along with $\Delta\mu_{a-\text{CW-NIRS}}$ traces (also normalized), from simultaneous measurements during six VA trials. The resumption of breathing is indicated by the gray shaded area [(D) and (E)], where a clear relative delay of $\Delta\mu_a$ relative to BFI is consistently observed. The falling edge lag between BFI and $\Delta\mu_{a-\text{fiDWS}}$, estimated as the maximum of the unbiased cross-correlation of rescaled waveforms within the gray shaded area, was 3.8 ± 1.6 s. This time lag is consistent with a delayed cerebrovascular "washout" effect (*54*). Note that the last 15 s of CW-NIRS data was unavailable in trial 3. (**F**) Scatter plot of $\Delta\mu_{a-\text{fiDWS}}$ and $\Delta\mu_{a-\text{CW-NIRS}}$ extracted from (E). Solid and dashed blue lines represent proportional fitting (slope of 1.04) and equality, respectively. ρ and ρ_c are Pearson and concordance correlation coefficients, respectively. (**G**) Bland-Altman plot shows the average (*x* axis) and difference (*y* axis) of $\Delta\mu_a$ measured by the two techniques.

NIRS, two modalities incur added cost and complexity. Here, we introduce the capability of fiDWS to perform optical absorption measurements and directly validate against CW-NIRS at a NIRS S-C separation of 3.5 cm that is commonly used for the adult brain (Fig. 4A). For validation against CW-NIRS, an MMF was positioned adjacent to the fiDWS collection fiber to collect diffuse light from a similar location. Collected CW intensity was directly monitored by an optical power meter (1936-R, Newport). Briefly, the CW intensity of fiDWS is extracted from the zero lag of the field autocorrelation [i.e., $G_1(0)$] (Fig. 4B) after noise correction (see Materials and Methods). This enables fiDWS to measure BFI and CW light intensity from a single S-C pair, using the same photons and optical path (Fig. 4B).

To validate the intrinsic multimodal capability of fiDWS, we investigated optical BFI and absorption responses of the human brain to voluntary apnea (VA), which can be considered as a simple and coarse method of assessing cerebrovascular reactivity (*52*). Respiratory CO_2 waveforms and oxygen saturation (SpO_2) were monitored by a capnometer and oximeter, respectively, during VA (Fig. 4C). For the example shown in Fig. 4C, a breath-holding period of ~55 s was determined from the duration of absence of the respiratory CO_2 waveform, where a higher end-tidal CO_2 ($etCO_2$) (~10 mmHg above baseline level) after resumption of breathing suggested an increase in the partial pressure of arterial CO_2 ($PaCO_2$). A large BFI increase of ~56% was measured by fiDWS in the VA trial (Fig. 4D). In general, absorption changes (from the differential modified Beer-Lambert law with a mean path length of ~25.7 cm) tracked BFI changes. Absorption changes from fiDWS ($\Delta\mu_{a\,-\,\mathrm{fiDWS}}$) and CW-NIRS ($\Delta\mu_{a\,-\,\mathrm{CW\,-\,NIRS}}$) are shown alongside rescaled BFI traces for six additional trials (Fig. 4E), where close correspondence between $\Delta\mu_{a\,-\,\mathrm{fiDWS}}$ and $\Delta\mu_{a\,-\,\mathrm{CW\,-\,NIRS}}$ is evident. Moreover, we found that absorption [which is 1.5 times higher for oxyhemoglobin than deoxyhemoglobin at the source wavelength of 852 nm; (*53*)] falling edges were generally delayed by a few seconds with respect to BFI falling edges (Fig. 4, D and E), consistent with the transit time of the cerebral vasculature (*54*). The agreement between $\Delta\mu_{a\,-\,\mathrm{fiDWS}}$ and $\Delta\mu_{a\,-\,\mathrm{CW\,-\,NIRS}}$ supports the ability of fiDWS to measure absorption changes (Fig. 4, F and G) in addition to BFI, without complex additional instrumentation.

Validation of fiDWS for CBF measurements

CBF is mediated by arterial blood pressure, intracranial pressure, and cerebrovascular resistance. CO_2 reactivity describes the relationship between the $PaCO_2$ and cerebrovascular tone (*52*). Intact CO_2 reactivity is a marker of cerebrovascular health and was applied here in healthy individuals to validate fiDWS as a measurement of CBF. Hypocapnia results in increased vascular tone and a decrease in CBF, whereas hypercapnia results in decreased vascular tone and an increase in CBF. To assess cerebrovascular reactivity more precisely than VA, we investigated BFI responses of the human brain to mild hypercapnia (Fig. 5A). A 3.5-cm S-C separation was chosen to afford high speed and brain specificity. Hypercapnia was achieved by inhaling medical air mixed with a low concentration of CO_2 (<5%), and fiDWS was synchronized with a capnometer and oximeter (see Materials and Methods). In healthy subjects, $etCO_2$ is an accurate estimate of $PaCO_2$ and is thus considered to be a suitable surrogate of $PaCO_2$ in blood (*55*), which regulates CBF. $EtCO_2$ traces were extracted from the upper envelope of the respiratory CO_2 waveform (Fig. 5B). Periods of hypercapnia lasted 60 s, with different inhaled CO_2 concentrations (i.e., lower envelope of the CO_2 waveform in Fig. 5B). Although the pulsatile BFI trace appears noisy, a clear BFI increase during hypercapnia is observed from the trace with a 10-s integration time (Fig. 5C).

Building on theoretical and experimental arguments supporting higher brain sensitivity of BFI fitted over earlier time lags (*39*), we assessed the ability of the zero lag autocorrelation derivative [i.e., $g_1'(0^+)$] to isolate brain BFI changes. As argued in section S4, even though $g_1(0) = 1$, the initial rate of decrease in g_1 provides BFI values that are specific to the brain. Rather than calculate the derivative of the raw data directly, we first performed a biexponential fit of the raw field autocorrelation [i.e., $G_1(\tau_d)$] and subsequently took a derivative analytically (see Materials and Methods). The biexponential fit provided an accurate empirical description of the early autocorrelation decay, and the analytical derivative strategy was less susceptible to noise than a direct numerical derivative. We found that the zero lag derivative could be described by a simple theoretical expression, enabling us to apply a double-layer model (section S4), along with reasonable assumptions of baseline anatomy and optical properties, to improve accuracy of BFI change estimates. The double-layer model served as a tool to roughly correct for the partial volume effect.

BFI measurements are known to be affected by both absorption and scattering (*56*). For simplicity, we assume constant scattering during hypercapnia. To estimate absorption changes related to hemodynamics, we used the previously validated CW intensity measurements of fiDWS (Fig. 5F), to account for absorption changes when fitting BFI and ultimately improve accuracy of relative blood flow changes. Initially, we assumed a mean path length of ~25.7 cm for a single-layer model. A delay in absorption with respect to BFI was observed during recovery from hypercapnia (Fig. 5F), as noted after VA (Fig. 4E), underscoring the complex temporal relationship between absorption and BFI changes.

A current standard practice is to use a semi-infinite DCS model to fit the "early" time lags (here, 0 to 42 μs) and recover BFI assuming a constant absorption. Relative to this standard practice, we found that three modifications measurably increased the recovered hyperemic BFI response during hypercapnia (Fig. 5E): (i) assessing the zero time lag derivative as opposed to fitting early time lags; (ii) using a double-layer model, instead of a semi-infinite model, to account for scalp BFI; and (iii) accounting for absorption changes during hypercapnia in the double-layer model. Graded BFI responses to $etCO_2$ changes, for 26 hypercapnic segments in three subjects (Fig. 5G), confirmed these observations. Accordingly, the double-layer zero lag derivative model, which provides highest brain specificity, with the inclusion of absorption compensation, shows a graded response of 3.2%/mmHg, ~2.5 times larger than the 1.3%/mmHg estimated by the semi-infinite DCS model. These results approach the 4 to 6% increase in CBF per mmHg ($PaCO_2$) reported by positron emission tomography (*57*, *58*). Furthermore, as shown in Fig. 5H, BFI changes from the semi-infinite DCS model correlate better with $etCO_2$ changes ($R^2 = 0.53$) than absorption changes ($R^2 = 0.09$), where R^2 is derived from a linear (slope and constant) fit. The zero lag derivative BFI models yield even higher correlations with $etCO_2$ changes, with R^2 ranging from 0.74 to 0.76.

As suggested by others (*59*, *60*), the shape of the pulsatile BFI waveform contains information about cerebrovascular tone and intracranial pressure. High-speed monitoring at 3.5-cm S-C separation provides a unique opportunity for analysis of a pulsatile waveform with intrinsically high-brain specificity. To assess pulsatility index (PI), we aligned BFI via a simultaneous pulse oximeter trace

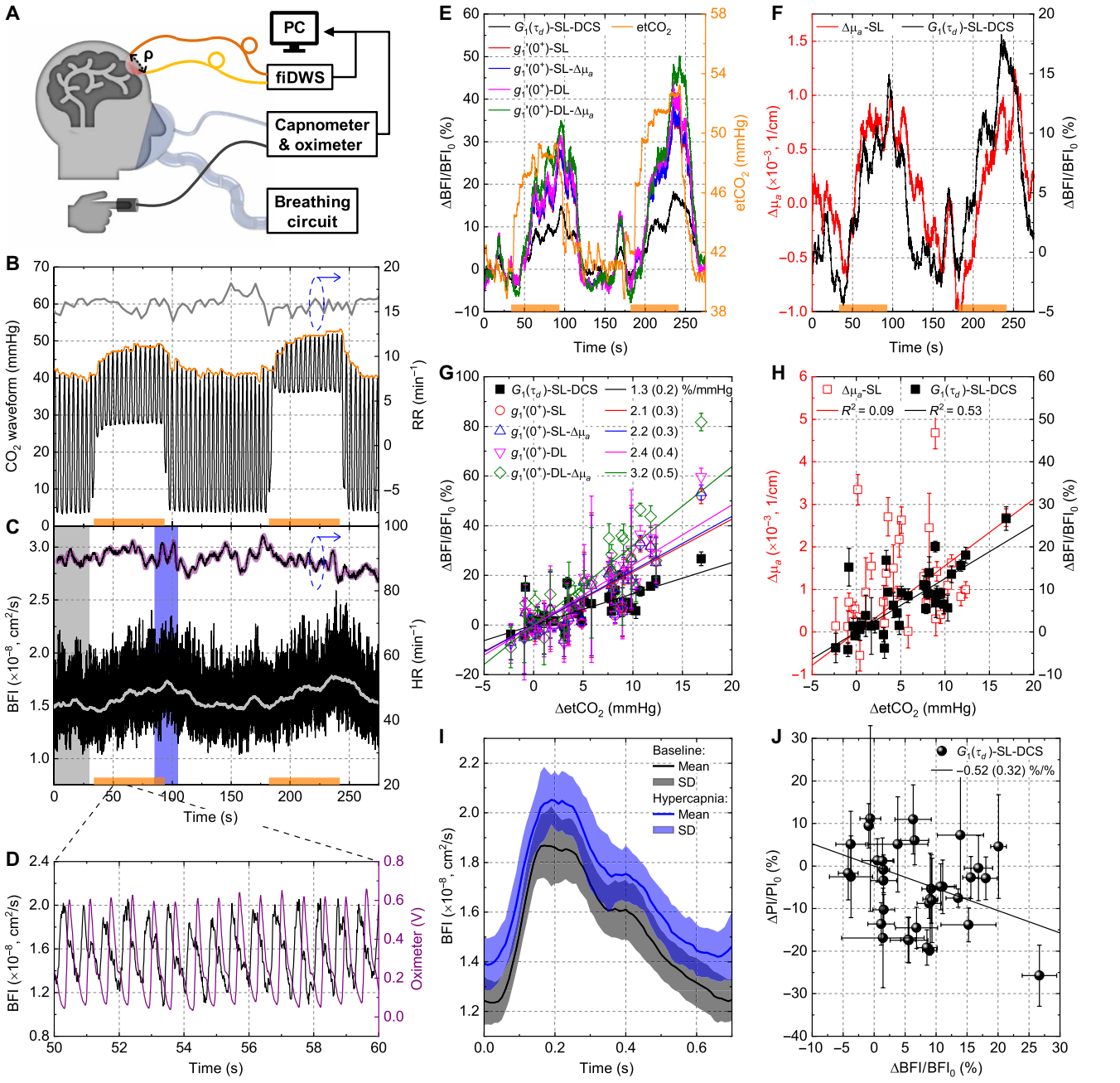

Fig. 5. Validation of fiDWS during mild hypercapnia at 3.5-cm S-C separation. (**A**) Experimental setup. (**B**) CO_2 waveform (black) and $etCO_2$ (orange upper envelope) during two periods of hypercapnia (orange bars along *x* axis). RR (gray) was estimated from the CO_2 waveform. (**C**) A single-layer (SL) DCS model with integration times of 0.1 and 10 s, respectively, yielded BFI traces with (black) and without (light gray) pulsatility. HR estimated from pulsatile BFI (black) and oximeter (purple) agrees. (**D**) Synchronized pulsatile BFI and oximeter traces. (**E**) Comparison of $etCO_2$ (right *y* axis) and BFI, estimated by one of five fitting models: a SL-DCS model, a single-layer $g_1'(0^+)$ (-SL) model without or with ($-\Delta\mu_a$) absorption compensation, and a double-layer $g_1'(0^+)$ (-DL) model without or with ($-\Delta\mu_a$) absorption compensation (see Materials and Methods and section S4). (**F**) Comparison of absorption and BFI determined by single-layer models. (**G**) Comparison of graded BFI responses to $etCO_2$ for all five models, across multiple trials and subjects, with proportional fit slopes and 95% confidence intervals in legend. (**H**) Comparison of graded absorption (SL) and BFI (SL-DCS) responses. Error bars in (G) and (H) indicate SDs within estimation windows (typically, 20 s around falling edge of $etCO_2$ trace). Solid lines indicate proportional fits ($Y = \alpha X$) [(G) and (H)]. Note that R^2 values were estimated from linear fits ($Y = \alpha X + \beta$). (**I**) Heartbeat-averaged BFI at baseline (black) and during hypercapnia (blue), indicated by shaded regions in (C) (SD, shaded SDs). (**J**) Hypercapnia-induced pulsatility index (PI) changes versus BFI changes from (H). The slope of a proportional fit was −0.52, with a 95% confidence interval of (−0.2 to −0.84). Error bars indicate SDs of $\Delta BFI/BFI_0$ and $\Delta PI/PI_0$.

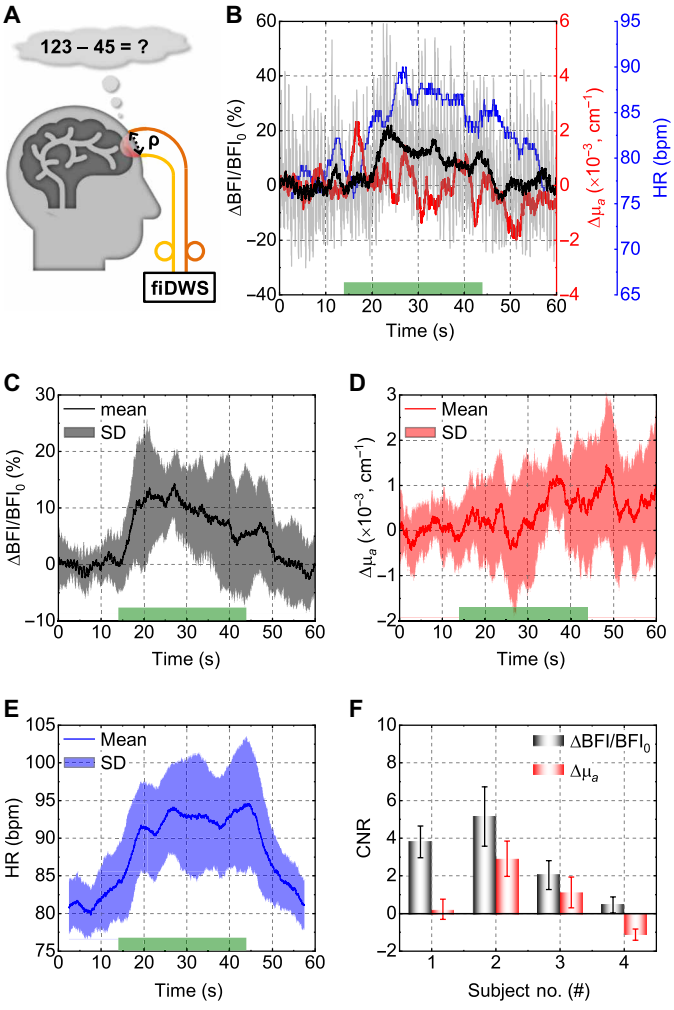

Fig. 6. fiDWS during prefrontal cortex activation. (**A**) Schematic of MA experiments. (**B**) Single trial changes in BFI with a 0.1-s integration time (light gray), BFI with a 2-s integration time (black), absorption (red), and HR (blue), the latter estimated from a short-time FFT of pulsatile BFI within a 5-s sliding window. The green bar on the *x* axis indicates the stimulus duration. (**C** to **E**) Averaged BFI (C), absorption (D), and HR (E) responses from multiple MA trials for one subject. Shading indicates SDs across trials. (**F**) The contrast-to-noise ratio (CNR) of BFI exceeds that of absorption for four subjects. Error bars indicate standard errors across trials. All BFIs in this figure were estimated by the SL-DCS model, with no absorption compensation.

(Fig. 5D), enabling separation of the pulsatile BFI trace into individual pulses (self-alignment is accurate for most pulsatile BFI traces at 3.5-cm S-C separation). Exemplary heartbeat-averaged BFI waveforms during baseline and hypercapnia (shaded regions in Fig. 5C) illustrate an increase in the mean BFI (Fig. 5I), with preservation of the waveform shape, pointing to a reduction in pulsatility. Changes in PI, assessed between the same baseline and hypercapnia regions, correlate negatively with changes in BFI [slope of −0.52 with 95% confidence intervals of (−0.2 to −0.84); Fig. 5J], consistent with previous work (*59*, *60*).

fiDWS for brain activation

CBF changes underlie numerous functional neuroimaging signals, including BOLD fMRI and functional CW-NIRS. We performed high-speed fiDWS monitoring of brain BFI during prefrontal cortex activation, achieved by a mental arithmetic (MA) task (*61*). An S-C separation of 3.5 cm was used to monitor pulsatile BFI (Fig. 6A). Consistent with previous reports (*62*, *63*), fiDWS shows an increase in BFI during brain activation. For the BFI trace with a 2-s integration time, activation is evident in single trials (Fig. 6B). On the basis of an averaged BFI trace from multiple trials for one subject (Fig. 6C), a rapid BFI increase of >10% occurred in first 5 s, followed by a slow decay and return to baseline level around 5 s after MA cessation. Corresponding averaged absorption changes, which are more susceptible to superficial and systemic contamination, show a weak correspondence with the stimulus (Fig. 6D). HR, directly estimated from pulsatile BFI traces, increased during MA (Fig. 6E), suggesting potential systemic physiological changes during the task. Yet, fiDWS of motor cortical activation (fig. S7) showed that BFI responses during finger tapping were not correlated to HR changes. Altogether, fiDWS achieved higher contrast-to-noise ratio (CNR) than CW-NIRS for all four subjects who performed MA (Fig. 6F). Thus, fiDWS can detect brain activation via optical BFI, measured at 3.5-cm S-C separation, providing both brain specificity and speed to observe cardiac pulsatility.

DISCUSSION

The field of optical BFI monitoring has long struggled with the trade-off between S-C separation, required for brain specificity, and light throughout required for SNR. In fiDWS, which detects the product of a weak sample field and a strong reference field, each pixel of the CMOS sensor approaches the shot noise–limited performance of a photon-counting channel (section S1). Since pixels are plentiful, a unique combination of S-C separation and speed is achieved, and cost per pixel (channel) is contained.

Incorporating a multitude of engineering advances needed for real-time monitoring, our fiDWS system continuously measures pulsatile BFI from the human forehead at S-C separations of 3.5 cm. For optical BFI monitoring, these results represent an unparalleled combination of speed and brain-to-scalp sensitivity. In one set of experiments, we assess cerebrovascular reactivity, showing a clear graded response of ~3.2 ± 0.5% BFI change per mmHg $etCO_2$. In another set of experiments, we show the time course of functional hyperemia, with pulsatility, during a MA task.

Using fiDWS to measure sample CW light intensity interferometrically, we compared simultaneous and coregistered absorption and BFI signals. Hypercapnia experiments revealed that $etCO_2$ changes were more correlated with BFI changes than with absorption changes, while MA experiments showed a higher CNR for BFI than absorption. These data lend experimental support to the theoretical predictions (*38*, *39*) that BFI is, inherently, a more brain-specific signal than absorption. Future studies will incorporate multiple wavelengths and compare optical BFI to hemoglobin concentrations.

The potential broader impact of optical brain monitoring technology is determined by performance-to-cost ratio. As a benchmark, avalanche photodiodes and correlator boards cost >$4000 per channel in DCS/DWS (*46*) [while recent work has shown the potential to parallelize photon counting with single-photon avalanche diode arrays, S-C separations of this approach remain relatively limited at the moment (*64*)]. By comparison, we estimate that the fiDWS approach, as implemented here, costs just ~$69 per speckle (two channels), based on ~$6600 for the camera and frame grabber (see Materials

and Methods), and $N_{\text{Noise speckle}}$ of ~96. Moreover, given the SNR benefits of field autocorrelations compared to intensity autocorrelations (*65*, *66*), the performance-to-cost advantage of fiDWS may be even higher. Such a reduction in the channel cost means that optical BFI is now a viable brain signal for studies of functional activation. Will fiDWS eventually be a serious competitor for functional CW-NIRS (or fNIRS) (*17*)? While the CMOS sensor in this work has a frame rate of several hundred kilohertz and hundreds of pixels, lower costs could be achieved by two-dimensional megapixel sensors with frame rates of several hundred hertz. The global CMOS sensor market, mainly based on such sensors, grew 14% in 2018 to reach $14.2 billion and is expected to exceed $20 billion by 2023 (*67*, *68*). With this in mind, on the same setup, we also investigated a multiexposure approach, which can be implemented on a camera with more pixels and a lower frame rate. The multiexposure approach yielded comparable results to the direct approach (section S10). Thus, our interferometric brain-sensing technology can potentially benefit from the robustness, low cost, and high performance driven by the growing worldwide market for detectors.

One possible concern about fiDWS is the stability of the MMF-based sample arm, which is sensitive to motion and vibrations. However, we find that fiDWS measurements are not susceptible to moderate motion of the MMF (movie S1), provided that the motional decorrelation dynamics are much slower than the intrinsic sample decorrelation dynamics.

In summary, fiDWS can assess optical BFI signals, driven either by neural activity or cerebrovascular reactivity, with an unmatched combination of speed and brain specificity. The methodology and its variants are projected to achieve increasingly competitive cost. Beyond monitoring in cardiac surgery, neurotrauma, ischemic stroke, and neonatal intensive care, fiDWS promises to facilitate assessing CBF at the point of care, in athletes or soldiers after head injury (*69*), and possibly even in portable devices that monitor brain activity.

MATERIALS AND METHODS

Experimental fiDWS setup

In our fiDWS system (Fig. 2A), the light source is an 852-nm distributed Bragg reflector laser with <1-MHz linewidth and >180-mW output power (D2-100-DBR-852-HP1, Vescent Photonics), driven by a 500-mA laser controller (D2-105-500, Vescent Photonics) with a power supply (D2-005, Vescent Photonics). The fiDWS system is based on a Mach-Zehnder interferometer, built from two fiber optic splitters. The first splitter, a fused SMF coupler (TW850R2A1, Thorlabs), splits 90 and 10% coupled laser power into sample and reference arms, respectively. In the sample arm, a collimated beam with a power of 50 mW over a spot size of >4 mm (i.e., $1/e^2$ beam diameter, adhering to the American National Standards Institute (ANSI) maximum permissible exposure of 4 mW/mm^2 at 852 nm) illuminates the scalp surface through a contact probe. Note that the maximum illumination power scales with the illumination spot area. Diffusively reflected light from the human forehead is collected by a contact MMF probe (QMMJ-3A2.5A-IRVIS-400/440-3PCBK-2, OZ Optics) at a distance ρ (S-C separation) away, where the MMF has a 400-μm core diameter and a 440-μm cladding diameter and a 0.22 NA. In the reference arm, a variable fiber-optic attenuator (BB-500-11-850-5/125-S-50-3A3A-1-1-ND-LL, OZ Optics) was used to adjust the mean reference light level to achieve the shot noise limit (section S1) while avoiding camera saturation (Fig. 2B). Before combining with sample light, the Gaussian intensity distribution of the collimated reference beam is converted into a uniform pattern in the horizontal direction using a Powell lens (#43-473, Edmund Optics). The horizontal dimension of the output beam is further truncated by an adjustable slit (VA100C, Thorlabs). Then, the reference beam is combined with the sample beam at second 90:10 free-space beam splitter (BS029, Thorlabs), where the sample arm has the larger output splitting ratio. Last, the combined light is focused onto a line-scan CMOS camera (spL4096-140km, Basler) with a quantum efficiency of >35% at 852 nm, via a cylindrical lens (AYL3026-B, Thorlabs) in the vertical direction. The camera is operated with a 333-kHz line rate for a region of interest of 512 horizontal pixels, with vertical pixel binning, and 4-tap/12-bit data acquisition. The cost breakdown of the fiDWS system can be found in table S1.

Estimation of field autocorrelation in fiDWS

In general, data processing can be divided into three steps (fig. S2): (i) Rolling mean subtraction: The raw signal of each pixel contains reference, sample, and heterodyne signals (i.e., $P_{\text{Tot}} = P_{\text{Ref}} + P_{\text{Sam}} + P_{\text{AC}}$). The sample light ($P_{\text{Sam}}$) is too weak for the CMOS sensor to detect, so this mean-subtracted signal, calculated using a 0.1-s rolling window, can be considered as equivalent to the heterodyne signal (P_{AC}), assuming the reference power (P_{Ref}) is stable over the window (note that the term "heterodyne" is used for P_{AC} owing to the large amplitudes difference between the sample and reference fields). (ii) Sliding pixel binning: Heterodyne signals over camera pixels are convolved with a Gaussian pixel binning function, which is approximately optimal (section S6). Binning coherently sums partially correlated pixels to improve the SNR. Where applicable, unless otherwise stated, we assume that the number of total binned pixels is equal to the number of camera pixels. (iii) Autocorrelation: Autocorrelation functions of individual binned pixels are calculated and summed (incoherent averaging).

Additive noise correction in N_{Speckle} estimation

In experiments, measured heterodyne signals consist of pure signal ($\mathbf{S}_p$) and additive noise ($\mathbf{N}_p$), where $\mathbf{N}_p$ is assumed to be a real, zero-mean, and independent Gaussian random variable for each pixel, typically resulting mostly from shot noise. To accurately quantify N_{Speckle} of the fiDWS system, a method to correct for overestimation of N_{Speckle} caused by additive noise is developed and used. The final equation for corrected N_{Speckle} is described as (see detailed derivation in section S8)

$$N_{\text{Speckle}} = \frac{\left(\langle \mathbf{I}_{S+N} \rangle - \langle \mathbf{I}_N \rangle\right)^2}{\text{var}(\mathbf{I}_{S+N}) - \text{var}(\mathbf{I}_N) - 4\sum_{p=1}^{P} \left[\left(\langle \mathbf{I}_{S+N,p} \rangle - \langle \mathbf{I}_{N,p} \rangle\right)\langle \mathbf{I}_{N,p} \rangle\right]} \quad (1)$$

where $\langle \mathbf{I}_{S+N} \rangle$ and $\langle \mathbf{I}_N \rangle$ are time-averaged intensity sums of noise-added (i.e., measured) heterodyne signal ($\mathbf{S}_p + \mathbf{N}_p$) and additive noise ($\mathbf{N}_p$) of pixels, respectively, $\langle \mathbf{I}_{S+N,p} \rangle$ and $\langle \mathbf{I}_{N,p} \rangle$ are corresponding time-averaged intensity for each pixel, P is total number of (binned) pixels, and var(·) indicates variance. Note that $\langle \mathbf{I}_N \rangle$, $\langle \mathbf{I}_{N,p} \rangle$, and var($\mathbf{I}_N$) can be either estimated from separate reference background measurements or the DC term (i.e., mean photon number), assuming that the shot noise limit has been achieved.

Models for fitting the field autocorrelation function

To extract BFI information from fiDWS estimates of the field autocorrelation function [i.e., $G_1(\tau_d)$], two models were used: (i) a DCS model and (ii) an empirical biexponential fitting model.

1) The DCS model, for fitting experimental $G_1(\tau_d)$, is expressed as

$$G_1(\tau_d) = A_1 g_1^{\mathrm{DCS}}(\tau_d) + A_2 \delta(\tau_d) \tag{2}$$

where the fitting coefficients A_1 and A_2 account for the amplitude of $G_1(\tau_d)$ and zero lag offset, respectively. Note that $g_1^{\mathrm{DCS}}(\tau_d)$ is the normalized DCS autocorrelation model. On the basis of the CW correlation diffusion equation, the normalized solution (i.e., normalized field autocorrelation), $g_1^{\mathrm{DCS}}(\tau_d)$, for a semi-infinite homogenous turbid medium with an S-C separation of ρ is given by (*70*)

$$g_1^{\mathrm{DCS}}(\tau_d) = \frac{r_2 \exp[-K(\tau_d) r_1] - r_1 \exp[-K(\tau_d) r_2]}{r_2 \exp[-K(0) r_1] - r_1 \exp[-K(0) r_2]} \tag{3}$$

where $K(\tau_d) = \sqrt{3\mu_a(\mu_s' + \mu_a)(1 + 2\mu_s' k^2 \alpha D_B \tau_d/\mu_a)}$, $r_1 = \sqrt{\rho^2 + z_0^2}$, $r_2 = \sqrt{\rho^2 + (z_0 + 2z_b)^2}$, $z_0 = 1/(\mu_s' + \mu_a)$, $z_b = 2(1 + R_{\mathrm{eff}})/[3(\mu_s' + \mu_a)(1 - R_{\mathrm{eff}})]$, $R_{\mathrm{eff}} = -1.44n^{-2} + 0.71n^{-1} + 0.668 + 0.064n$, n is the ratio of refractive indices between the medium and air, k is the wave number of the light propagating in the medium, μ_s' is the reduced scattering coefficient, and μ_a is the absorption coefficient. For liquid phantoms, D_B is the Brownian diffusion coefficient of moving scatters and $\alpha = 1$, while for biological tissues, the term of αD_B is referred to as BFI, where the unitless factor α accounts for static scatters in the tissue. Empirically, BFI correlates with blood flow (*21*, *71*).

2) The empirical biexponential model (*72*), used for estimating the zero time lag derivative [i.e., $g_1'(0^+)$], is

$$G_1(\tau_d) = B_1 \exp\left(-\frac{\tau_d}{\tau_{c1}}\right) + B_2 \exp\left(-\frac{\tau_d}{\tau_{c2}}\right) + B_3 \delta(\tau_d) \tag{4}$$

where the fitting coefficients B_1, B_2, and B_3 account for amplitudes of two decay components and zero lag offset, respectively, and τ_{c1} and τ_{c2} are decay times of two exponential components. Note that inclusion of a delta function at zero lag ($\tau_d = 0$) is equivalent to excluding the zero lag from the fit. The analytical expression for $g_1'(0^+)$ can be written as

$$g_1'(0^+) = \frac{B_1 \tau_{c2} + B_2 \tau_{c1}}{(B_1 + B_2)\tau_{c1}\tau_{c2}} \tag{5}$$

On the basis of the double-layer derivative model (section S4), expressed as

$$g_1'(0^+) = -2k^2[\alpha_1 D_{B1} \mu_{s1}' \overline{l_1} + \alpha_2 D_{B2} \mu_{s2}' \overline{l_2}] \tag{6}$$

where k is the medium wave number, and $\overline{l_1}$ and $\overline{l_2}$ are the partial path lengths of extracerebral and cerebral layers, respectively, the brain BFI ($\alpha_2 D_{B2}$) can be estimated. We assume that $\alpha_1 D_{B1} = 10^{-9}$ cm^2/s, $\mu_{s1}' = 12$ cm^{-1}, and $\mu_{s2}' = 12$ cm^{-1} for the human head (*38*). Moreover, $\overline{l_1}$ and $\overline{l_2}$ are obtained from Monte Carlo simulation, where $\overline{l_2}$ can be further corrected for absorption changes (absorption compensation). For the single-layer derivative model, expressed as

$$g_1'(0^+) = -2k^2 \alpha D_B \mu_s' \bar{l} \tag{7}$$

BFI can be simply estimated (see more details in section S4). For this model, relative BFI changes are equal to relative $g_1'(0^+)$ changes if optical properties do not change.

Noise correction of $G_1(0)$

The raw experimental $G_1(\tau_d)$ includes a zero lag offset, consisting of noise variances from the camera (σ_{Cam}^2) and reference light (σ_{Shot}^2). This offset must be corrected to accurately estimate CW intensity. The constant σ_{Cam}^2 can be directly estimated from separate camera background measurements. However, since the reference intensity tends to drift over time (possibly due to polarization drift in the reference fiber), the shot noise variance must be estimated from the contemporaneously estimated reference intensity (I_{Ref}). Specifically, $\sigma_{\mathrm{Shot}}^2 = I_{\mathrm{Ref}}/(\mathrm{FWC}/4096)$, where FWC is the calibrated full well capacity (section S1) of the 4096 level CMOS camera. $G_1(0)$ is corrected by subtracting both σ_{Shot}^2 and σ_{Cam}^2.

Human subjects

For this study, five healthy adult human subjects (aged 25 to 66 years) were recruited for VA, hypercapnia, MA, and finger-tapping measurements. Informed consent was obtained from all subjects. All experimental procedures and protocols involving human subject research were reviewed and approved by the University of California Davis Institutional Review Board, and safety precautions (e.g., laser safety goggles, beam blocks, and protective screens) were implemented to avoid accidental eye exposure from laser.

Breathing circuit and gas delivery for hypercapnia

The gas delivery apparatus, used for modulating CO_2 content of inspired air to induce hypercapnia, consists of a gas blender, breathing circuit, and CO_2 monitor. A clinical air-oxygen blender (PM5200, Precision Medical) is used to blend adjustable amounts of pure medical air and a 5% CO_2–medical air mixture (i.e., 5% CO_2, 20% O_2, and 75% N_2). The output gas mixture, with an adjustable CO_2 concentration (0 to 5%), is then delivered to a breathing circuit. Details of the breathing circuit are described in (*73*). A capnograph (9004051, Smiths Medical) with oximeter capabilities was used to monitor CO_2 concentration of respiratory gas. Analog output signals of the capnograph, including respiratory CO_2 waveform, etCO_2 trace, and pulse oximetry, were acquired by a Data Acquisition (DAQ) card (PCIe-6363, National Instruments). Last, the frame grabber (PCIe-1433, National Instruments) used for the fiDWS camera was synchronized with DAQ card to achieve multiparameter monitoring during hypercapnia.

MA protocol

Each subject was instructed to sit still and think about nothing for a resting period of 10 min before multiple (≥5) trials of MA. The fiDWS optical probe was secured over left prefrontal cortex region on forehead. In each trial, subjects were asked to solve math problems as fast as they could (but without a time limit for each question) for a total duration of 30 s, followed by a few minutes of rest. All math problems were based on subtraction of a two-digit number from a three-digit number with borrowing (e.g., 123 − 45 = ?).

SUPPLEMENTARY MATERIALS

Supplementary material for this article is available at http://advances.sciencemag.org/cgi/content/full/7/20/eabe0150/DC1

REFERENCES AND NOTES

1. C.-Y. Xing, T. Tarumi, J. Liu, Y. Zhang, M. Turner, J. Riley, C. D. Tinajero, L.-J. Yuan, R. Zhang, Distribution of cardiac output to the brain across the adult lifespan. *J. Cereb. Blood Flow Metab.* **37**, 2848–2856 (2017).
2. H. S. Markus, Cerebral perfusion and stroke. *J. Neurol.* **75**, 353–361 (2004).
3. A. Morotti, G. Busto, A. Bernardoni, S. Marini, I. Casetta, E. Fainardi, Association between perihematomal perfusion and intracerebral hemorrhage outcome. *Neurocrit. Care* **33**, 525–532 (2020).
4. G. J. Bouma, J. P. Muizelaar, Cerebral blood flow, cerebral blood volume, and cerebrovascular reactivity after severe head injury. *J. Neurotrauma* **9** (Suppl. 1), S333–S348 (1992).
5. H. Engquist, E. Rostami, P. Enblad, Temporal dynamics of cerebral blood flow during the acute course of severe subarachnoid hemorrhage studied by bedside xenon-enhanced CT. *Neurocrit. Care* **30**, 280–290 (2019).
6. P. T. Fox, M. E. Raichle, M. A. Mintun, C. Dence, Nonoxidative glucose consumption during focal physiologic neural activity. *Science* **241**, 462–464 (1988).
7. N. K. Logothetis, J. Pauls, M. Augath, T. Trinath, A. Oeltermann, Neurophysiological investigation of the basis of the fMRI signal. *Nature* **412**, 150–157 (2001).
8. K. K. Kwong, J. W. Belliveau, D. A. Chesler, I. E. Goldberg, R. M. Weisskoff, B. P. Poncelet, D. N. Kennedy, B. E. Hoppel, M. S. Cohen, R. Turner, Dynamic magnetic resonance imaging of human brain activity during primary sensory stimulation. *Proc. Natl. Acad. Sci. U.S.A.* **89**, 5675–5679 (1992).
9. S. Ogawa, D. W. Tank, R. Menon, J. M. Ellermann, S. G. Kim, H. Merkle, K. Ugurbil, Intrinsic signal changes accompanying sensory stimulation: Functional brain mapping with magnetic resonance imaging. *Proc. Natl. Acad. Sci. U.S.A.* **89**, 5951–5955 (1992).
10. K. N. Kay, T. Naselaris, R. J. Prenger, J. L. Gallant, Identifying natural images from human brain activity. *Nature* **452**, 352–355 (2008).
11. E. Rostami, H. Engquist, P. Enblad, Imaging of cerebral blood flow in patients with severe traumatic brain injury in the neurointensive care. *Front. Neurol.* **5**, 114 (2014).
12. D. B. Douglas, R. Chaudhari, J. M. Zhao, J. Gullo, J. Kirkland, P. K. Douglas, E. Wolin, J. Walroth, M. Wintermark, Perfusion imaging in acute traumatic brain injury. *Neuroimaging Clin. N. Am.* **28**, 55–65 (2018).
13. S.-p. Peng, Y.-n. Li, J. Liu, Z.-y. Wang, Z.-s. Zhang, S.-k. Zhou, F.-x. Tao, Z.-x. Zhang, Pulsed arterial spin labeling effectively and dynamically observes changes in cerebral blood flow after mild traumatic brain injury. *Neural Regen. Res.* **11**, 257–261 (2016).
14. G. Rosenthal, R. O. Sanchez-Mejia, N. Phan, J. C. Hemphill III, C. Martin, G. T. Manley, Incorporating a parenchymal thermal diffusion cerebral blood flow probe in bedside assessment of cerebral autoregulation and vasoreactivity in patients with severe traumatic brain injury. *J. Neurosurg.* **114**, 62–70 (2011).
15. P. Blanco, A. Abdo-Cuza, Transcranial Doppler ultrasound in neurocritical care. *J. Ultrasound* **21**, 1–16 (2018).
16. F. F. Jöbsis, Noninvasive, infrared monitoring of cerebral and myocardial oxygen sufficiency and circulatory parameters. *Science* **198**, 1264–1267 (1977).
17. A. T. Eggebrecht, S. L. Ferradal, A. Robichaux-Viehoever, M. S. Hassanpour, H. Dehghani, A. Z. Snyder, T. Hershey, J. P. Culver, Mapping distributed brain function and networks with diffuse optical tomography. *Nat. Photonics* **8**, 448–454 (2014).
18. S. Lloyd-Fox, A. Blasi, C. E. Elwell, Illuminating the developing brain: The past, present and future of functional near infrared spectroscopy. *Neurosci. Biobehav. Rev.* **34**, 269–284 (2010).
19. R. Bonner, R. Nossal, Model for laser Doppler measurements of blood flow in tissue. *Appl. Optics* **20**, 2097–2107 (1981).
20. D. A. Boas, A. G. Yodh, Spatially varying dynamical properties of turbid media probed with diffusing temporal light correlation. *J. Opt. Soc. Am. A* **14**, 192–215 (1997).
21. T. Durduran, A. G. Yodh, Diffuse correlation spectroscopy for non-invasive, micro-vascular cerebral blood flow measurement. *Neuroimage* **85** (Pt. 1), 51–63 (2014).
22. E. M. Buckley, N. M. Cook, T. Durduran, M. N. Kim, C. Zhou, R. Choe, G. Yu, S. Schultz, C. M. Sehgal, D. J. Licht, P. H. Arger, M. E. Putt, H. H. Hurt, A. G. Yodh, Cerebral hemodynamics in preterm infants during positional intervention measured with diffuse correlation spectroscopy and transcranial Doppler ultrasound. *Opt. Express* **17**, 12571–12581 (2009).
23. G. Yu, T. F. Floyd, T. Durduran, C. Zhou, J. Wang, J. A. Detre, A. G. Yodh, Validation of diffuse correlation spectroscopy for muscle blood flow with concurrent arterial spin labeled perfusion MRI. *Opt. Express* **15**, 1064–1075 (2007).
24. N. Roche-Labarbe, S. A. Carp, A. Surova, M. Patel, D. A. Boas, P. E. Grant, M. A. Franceschini, Noninvasive optical measures of CBV, StO(2), CBF index, and rCMRO(2) in human premature neonates' brains in the first six weeks of life. *Hum. Brain Mapp.* **31**, 341–352 (2010).
25. N. Roche-Labarbe, A. Fenoglio, A. Aggarwal, M. Dehaes, S. A. Carp, M. A. Franceschini, P. E. Grant, Near-infrared spectroscopy assessment of cerebral oxygen metabolism in the developing premature brain. *J. Cereb. Blood Flow Metab.* **32**, 481–488 (2012).
26. M. Diop, K. Verdecchia, T.-Y. Lee, K. St. Lawrence, Calibration of diffuse correlation spectroscopy with a time-resolved near-infrared technique to yield absolute cerebral blood flow measurements. *Biomed. Opt. Express* **2**, 2068–2081 (2011).
27. E. M. Buckley, D. Hance, T. Pawlowski, J. Lynch, F. B. Wilson, R. C. Mesquita, T. Durduran, L. K. Diaz, M. E. Putt, D. J. Licht, M. A. Fogel, A. G. Yodh, Validation of diffuse correlation spectroscopic measurement of cerebral blood flow using phase-encoded velocity mapping magnetic resonance imaging. *J. Biomed. Opt.* **17**, 037007 (2012).
28. Q. Zhang, E. N. Brown, G. E. Strangman, Adaptive filtering to reduce global interference in evoked brain activity detection: A human subject case study. *J. Biomed. Opt.* **12**, 064009 (2007).
29. J. Selb, K.-C. Wu, J. Sutin, P.-Y. I. Lin, P. Farzam, S. Bechek, A. Shenoy, A. B. Patel, D. A. Boas, M. A. Franceschini, E. S. Rosenthal, Prolonged monitoring of cerebral blood flow and autoregulation with diffuse correlation spectroscopy in neurocritical care patients. *Neurophotonics* **5**, 045005 (2018).
30. W. B. Baker, A. B. Parthasarathy, T. S. Ko, D. R. Busch, K. Abramson, S. Y. Tzeng, R. C. Mesquita, T. Durduran, J. H. Greenberg, D. K. Kung, A. G. Yodh, Pressure modulation algorithm to separate cerebral hemodynamic signals from extracerebral artifacts. *Neurophotonics* **2**, 035004 (2015).
31. A. B. Parthasarathy, K. P. Gannon, W. B. Baker, C. G. Favilla, R. Balu, S. E. Kasner, A. G. Yodh, J. A. Detre, M. T. Mullen, Dynamic autoregulation of cerebral blood flow measured non-invasively with fast diffuse correlation spectroscopy. *J. Cereb. Blood Flow Metab.* **38**, 230–240 (2018).
32. R. B. Saager, A. J. Berger, Measurement of layer-like hemodynamic trends in scalp and cortex: Implications for physiological baseline suppression in functional near-infrared spectroscopy. *J. Biomed. Opt.* **13**, 034017 (2008).
33. M. Pagliazzi, S. K. V. Sekar, L. Colombo, E. Martinenghi, J. Minnema, R. Erdmann, D. Contini, A. D. Mora, A. Torricelli, A. Pifferi, T. Durduran, Time domain diffuse correlation spectroscopy with a high coherence pulsed source: In vivo and phantom results. *Biomed. Opt. Express* **8**, 5311–5325 (2017).
34. J. Sutin, B. Zimmerman, D. Tyulmankov, D. Tamborini, K. C. Wu, J. Selb, A. Gulinatti, I. Rech, A. Tosi, D. A. Boas, M. A. Franceschini, Time-domain diffuse correlation spectroscopy. *Optica* **3**, 1006–1013 (2016).
35. A. Tsalach, Z. Schiffer, E. Ratner, I. Breskin, R. Zeitak, R. Shechter, M. Balberg, Depth selective acousto-optic flow measurement. *Biomed. Opt. Express* **6**, 4871–4886 (2015).
36. H. W. Schytz, S. Guo, L. T. Jensen, M. Kamar, A. Nini, D. R. Gress, M. Ashina, A new technology for detecting cerebral blood flow: A comparative study of ultrasound tagged NIRS and ^{133}Xe-SPECT. *Neurocrit. Care* **17**, 139–145 (2012).
37. A. Hussain, W. Steenbergen, I. M. Vellekoop, Imaging blood flow inside highly scattering media using ultrasound modulated optical tomography. *J. Biophotonics* **11**, e201700013 (2018).
38. J. Selb, D. A. Boas, S.-T. Chan, K. C. Evans, E. M. Buckley, S. A. Carp, Sensitivity of near-infrared spectroscopy and diffuse correlation spectroscopy to brain hemodynamics: Simulations and experimental findings during hypercapnia. *Neurophotonics* **1**, 015005 (2014).
39. W. B. Baker, A. B. Parthasarathy, D. R. Busch, R. C. Mesquita, J. H. Greenberg, A. G. Yodh, Modified Beer-Lambert law for blood flow. *Biomed. Opt. Express* **5**, 4053–4075 (2014).
40. M. A. Yücel, J. J. Selb, T. J. Huppert, M. A. Franceschini, D. A. Boas, Functional near infrared spectroscopy: Enabling routine functional brain imaging. *Curr. Opin. Biomed. Eng.* **4**, 78–86 (2017).
41. L. He, Y. Lin, Y. Shang, B. J. Shelton, G. Yu, Using optical fibers with different modes to improve the signal-to-noise ratio of diffuse correlation spectroscopy flow-oximeter measurements. *J. Biomed. Opt.* **18**, 037001 (2013).
42. D. Wang, A. B. Parthasarathy, W. B. Baker, K. Gannon, V. Kavuri, T. Ko, S. Schenkel, Z. Li, Z. Li, M. T. Mullen, J. A. Detre, A. G. Yodh, Fast blood flow monitoring in deep tissues with real-time software correlators. *Biomed. Opt. Express* **7**, 776–797 (2016).
43. G. Dietsche, M. Ninck, C. Ortolf, J. Li, F. Jaillon, T. Gisler, Fiber-based multispeckle detection for time-resolved diffusing-wave spectroscopy: Characterization and application to blood flow detection in deep tissue. *Appl. Optics* **46**, 8506–8514 (2007).
44. L. Gagnon, M. A. Yücel, D. A. Boas, R. J. Cooper, Further improvement in reducing superficial contamination in NIRS using double short separation measurements. *Neuroimage* **85** (Pt. 1), 127–135 (2014).
45. W. Zhou, O. Kholiqov, S. P. Chong, V. J. Srinivasan, Highly parallel, interferometric diffusing wave spectroscopy for monitoring cerebral blood flow dynamics. *Optica* **5**, 518–527 (2018).
46. C. Huang, M. Seong, J. P. Morgan, S. Mazdeyasna, J. G. Kim, J. T. Hastings, G. Yu, Low-cost compact diffuse speckle contrast flowmeter using small laser diode and bare charge-coupled-device. *J. Biomed. Opt.* **21**, 080501 (2016).
47. R. Cheng, Y. Shang, S. Wang, J. M. Evans, A. Rayapati, D. C. Randall, G. Yu, Near-infrared diffuse optical monitoring of cerebral blood flow and oxygenation for the prediction of vasovagal syncope. *J. Biomed. Opt.* **19**, 17001 (2014).
48. Y. Hou, Y. Shang, R. Cheng, Y. Zhao, Y. Qin, R. Kryscio, A. Rayapati, D. Hayes, G. Yu, Obstructive sleep apnea–hypopnea results in significant variations in cerebral

hemodynamics detected by diffuse optical spectroscopies. *Physiol. Meas.* **35**, 2135–2148 (2014).
49. Y. Fukui, Y. Ajichi, E. Okada, Monte Carlo prediction of near-infrared light propagation in realistic adult and neonatal head models. *Appl. Optics* **42**, 2881–2887 (2003).
50. G. E. Strangman, Z. Li, Q. Zhang, Depth sensitivity and source-detector separations for near infrared spectroscopy based on the Colin27 brain template. *PLOS ONE* **8**, e66319 (2013).
51. D. Tamborini, P. Farzam, B. Zimmermann, K.-C. Wu, D. A. Boas, M. A. Franceschini, Development and characterization of a multidistance and multiwavelength diffuse correlation spectroscopy system. *Neurophotonics* **5**, 011015 (2017).
52. J. Fierstra, O. Sobczyk, A. Battisti-Charbonney, D. M. Mandell, J. Poublanc, A. P. Crawley, D. J. Mikulis, J. Duffin, J. A. Fisher, Measuring cerebrovascular reactivity: What stimulus to use? *J. Physiol.* **591**, 5809–5821 (2013).
53. Y. Zhao, L. Qiu, Y. Sun, C. Huang, T. Li, Optimal hemoglobin extinction coefficient data set for near-infrared spectroscopy. *Biomed. Opt. Express* **8**, 5151–5159 (2017).
54. M. Ibaraki, H. Ito, E. Shimosegawa, H. Toyoshima, K. Ishigame, K. Takahashi, I. Kanno, S. Miura, Cerebral vascular mean transit time in healthy humans: A comparative study with PET and dynamic susceptibility contrast-enhanced MRI. *J. Cereb. Blood Flow Metab.* **27**, 404–413 (2007).
55. Y. Takano, O. Sakamoto, C. Kiyofuji, K. Ito, A comparison of the end-tidal CO_2 measured by portable capnometer and the arterial $P\,CO_2$ in spontaneously breathing patients. *Respir. Med.* **97**, 476–481 (2003).
56. D. Irwin, L. Dong, Y. Shang, R. Cheng, M. Kudrimoti, S. D. Stevens, G. Yu, Influences of tissue absorption and scattering on diffuse correlation spectroscopy blood flow measurements. *Biomed. Opt. Express* **2**, 1969–1985 (2011).
57. H. Ito, I. Kanno, M. Ibaraki, J. Hatazawa, S. Miura, Changes in human cerebral blood flow and cerebral blood volume during hypercapnia and hypocapnia measured by positron emission tomography. *J. Cereb. Blood Flow Metab.* **23**, 665–670 (2003).
58. G. E. Cold, Cerebral blood flow in acute head injury. The regulation of cerebral blood flow and metabolism during the acute phase of head injury, and its significance for therapy. *Acta Neurochir. Suppl.* **49**, 1–64 (1990).
59. A.-M. Homburg, M. Jakobsen, E. Enevoldsen, Transcranial doppler recordings in raised intracranial pressure. *Acta Neurol. Scand.* **87**, 488–493 (1993).
60. M. Czosnyka, H. K. Richards, H. E. Whitehouse, J. D. Pickard, Relationship between transcranial Doppler-determined pulsatility index and cerebrovascular resistance: An experimental study. *J. Neurosurg.* **84**, 79–84 (1996).
61. N. Naseer, K.-S. Hong, fNIRS-based brain-computer interfaces: A review. *Front. Hum. Neurosci.* **9**, 3 (2015).
62. T. Durduran, G. Yu, M. G. Burnett, J. A. Detre, J. H. Greenberg, J. Wang, C. Zhou, A. G. Yodh, Diffuse optical measurement of blood flow, blood oxygenation, and metabolism in a human brain during sensorimotor cortex activation. *Opt. Lett.* **29**, 1766–1768 (2004).
63. J. Li, G. Dietsche, D. Iftime, S. E. Skipetrov, G. Maret, T. Elbert, B. Rockstroh, T. Gisler, Noninvasive detection of functional brain activity with near-infrared diffusing-wave spectroscopy. *J. Biomed. Opt.* **10**, 044002 (2005).
64. W. Liu, R. Qian, S. Xu, P. C. Konda, J. Jönsson, M. Harfouche, D. Borycki, C. Cooke, E. Berrocal, Q. Dai, H. Wang, R. Horstmeyer, Fast and sensitive diffuse correlation spectroscopy with highly parallelized single photon detection. *APL Photonics* **6**, 026106 (2021).
65. D. Borycki, O. Kholiqov, V. J. Srinivasan, Interferometric near-infrared spectroscopy directly quantifies optical field dynamics in turbid media. *Optica* **3**, 1471–1476 (2016).
66. M. B. Robinson, D. A. Boas, S. Sakadžic, M. A. Franceschini, S. A. Carp, Interferometric diffuse correlation spectroscopy improves measurements at long source–detector separation and low photon count rate. *J. Biomed. Opt.* **25**, 097004 (2020).
67. P. Clarke, "CMOS image sensor market keeps on growing," 28 August 2019; www.eenewsanalog.com/news/cmos-image-sensor-market-keeps-growing.
68. P. Clarke, "CMOS image sensor market to grow 10.1 percent in 2019," 11 July 2019; www.eenewsanalog.com/news/cmos-image-sensor-market-grow-101-percent-2019#:~:text=The%20CMOS%20image%20sensor%20market,2019's%20market%20at%20%2417%20billion.
69. J. A. Stephens, P. Liu, H. Lu, S. J. Suskauer, Cerebral blood flow after mild traumatic brain injury: Associations between symptoms and post-injury perfusion. *J. Neurotrauma* **35**, 241–248 (2018).
70. T. Durduran, R. Choe, W. B. Baker, A. G. Yodh, Diffuse optics for tissue monitoring and tomography. *Rep. Prog. Phys.* **73**, 076701 (2010).
71. E. M. Buckley, A. B. Parthasarathy, P. E. Grant, A. G. Yodh, M. A. Franceschini, Diffuse correlation spectroscopy for measurement of cerebral blood flow: Future prospects. *Neurophotonics* **1**, 011009 (2014).
72. O. Kholiqov, W. Zhou, T. Zhang, V. N. Du Le, V. J. Srinivasan, Time-of-flight resolved light field fluctuations reveal deep human tissue physiology. *Nat. Commun.* **11**, 391 (2020).
73. F. B. Tancredi, I. Lajoie, R. D. Hoge, A simple breathing circuit allowing precise control of inspiratory gases for experimental respiratory manipulations. *BMC. Res. Notes* **7**, 235 (2014).
74. D. J. Pine, D. A. Weitz, P. M. Chaikin, E. Herbolzheimer, Diffusing wave spectroscopy. *Phys. Rev. Lett.* **60**, 1134–1137 (1988).
75. F. Martelli, S. D. Bianco, A. Ismaelli, G. Zaccanti, The Radiative Transfer Equation and Diffusion Equation, in *Light Propagation through Biological Tissue and Other Diffusive Media: Theory, Solutions, and Software* (SPIE Press, Bellingham, Washington, USA, 2009), pp. 29–54.
76. L. Yu, F. Nina-Paravecino, D. Kaeli, Q. Fang, Scalable and massively parallel Monte Carlo photon transport simulations for heterogeneous computing platforms. *J. Biomed. Opt.* **23**, 010504 (2018).
77. R. C. Mesquita, S. S. Schenkel, D. L. Minkoff, X. Lu, C. G. Favilla, P. M. Vora, D. R. Busch, M. Chandra, J. H. Greenberg, J. A. Detre, A. G. Yodh, Influence of probe pressure on the diffuse correlation spectroscopy blood flow signal: Extra-cerebral contributions. *Biomed. Opt. Express* **4**, 978–994 (2013).

Acknowledgments: We thank A. Kho for help in building the gas delivery system. **Funding:** This work was supported by NIH grants R01EB029747, R01EY031469, R01NS094681, R21NS105043, and R03EB023591. **Author contributions:** W.Z. built the fiDWS system, performed the experiments, and processed the data. W.Z. and V.J.S. developed the data acquisition program and data processing method. V.J.S. performed the theoretical analysis and simulations. O.K. contributed to the experimental design and data processing. J.Z. and B.G.L. contributed to the hypercapnia experiments. M.Z. contributed to the finger-tapping experiments. L.L.Z., R.M.M., and B.G.L. contributed to the design of human experiments. W.Z. and V.J.S. conceived the project and wrote the manuscript. All authors were involved in discussions and contributed to the manuscript editing. V.J.S. supervised the project. **Competing interests:** W.Z., O.K., and V.J.S. are inventors on a patent application related to this work filed by the University of California (no. WO2019204231A1, filed 15 April 2019). The other authors declare that they have no competing interests. **Data and materials availability:** All data needed to evaluate the conclusions in the paper are present in the paper and/or the Supplementary Materials. Additional data related to this paper may be requested from the authors.

Submitted 25 July 2020
Accepted 23 March 2021
Published 12 May 2021
10.1126/sciadv.abe0150

Citation: W. Zhou, O. Kholiqov, J. Zhu, M. Zhao, L. L. Zimmermann, R. M. Martin, B. G. Lyeth, V. J. Srinivasan, Functional interferometric diffusing wave spectroscopy of the human brain. *Sci. Adv.* **7**, eabe0150 (2021).